ORIGINAL ARTICLE

Reduced graphene oxide/polypyrrole composite: an advanced electrode for high-performance symmetric/asymmetric supercapacitor

Guijing Liu[1,2] · Yanying Shi[1] · Lei Wang[3] · Yadong Song[1] · Shanmin Gao[1] · Dong Liu[1] · Leqing Fan[2]

Abstract

Polypyrrole (PPy) decorated on reduced graphene oxide (rGO) films is successfully prepared with pyrrole (Py) monomers and rGO through one-step combining oxidation with polymerization reaction. Compared with the pure individual components, rGO/PPy compound turns out better electrochemical characteristics owing to the introduction of rGO sheets, which improves the specific surface area and the conductivity of composite material. When the amount of rGO is 10% of the total, the rGO/PPy compound delivers the best capacitance of 389.3 F g^{-1} at 1.0 A g^{-1} in a three-electrode system and 266.8 F g^{-1} at 0.25 A g^{-1} in the symmetric supercapacitor system. In addition, asymmetric device (rGO/PPy//AC) has been successfully fabricated using optimized rGO/PPy compound as positive electrode, activated carbon as negative electrode (AC) and 1 M Na$_2$SO$_4$ aqueous solution as electrolyte. The device obtains long cycle stability under the high-voltage region from 0 to 1.6 V, meanwhile displaying the satisfied energy density of 19.7 Wh kg^{-1} at 478.1 W kg^{-1}. Besides, the rGO/PPy//AC device presents satisfactory rate capability and long life time.

Keywords Reduced graphene oxide · Asymmetric supercapacitor · Polypyrrole · Compound

1 Introduction

Supercapacitors featuring high power density, shot charging time, low cost, low pollution and long lifetime reveal a huge potential for applications in energy devices [1–4]. In

✉ Guijing Liu
  liu_guijing@163.com

✉ Leqing Fan
  leqingfan@163.com

1 School of Chemistry and Materials Science, Ludong University, Yantai 264025, People's Republic of China

2 Engineering Research Center of Environment-Friendly Functional Materials, Ministry of Education, College of Materials Science and Engineering, Huaqiao University, Xiamen 361021, Fujian, People's Republic of China

3 MIIT Key Laboratory of Critical Materials Technology for New Energy Conversion and Storage, School of Chemistry and Chemical Engineering, Harbin Institute of Technology, Harbin 150001, People's Republic of China

particular, asymmetric supercapacitors with high rate and cyclic reversibility have emerged as an appealing strategy to satisfy the increasing demands of energy storage systems [5]. However, compared with the rechargeable batteries, supercapacitors exhibit relatively low energy density restrained by the specific capacitance and cell voltage, which severely impede their practical utilization [6, 7]. As a consequence, a great amount of effort has been devoted to improving the energy density without degrading other excellent features [8, 9]. It is well known that designing and developing advanced positive/negative electrode is of great importance to achieve the desired performance in the same electrolyte under different potential windows. Carbonaceous materials, such as carbon nanotubes (CNTs), activated carbon (AC), carbon aerogel and graphene, are generally served as the negative electrodes. Because AC at the interface of electrode and electrolytes easily forms a large amount of more layers, which can accelerate the ions transport in the electrolyte, resulting in a high rate capability as well as an improved energy storage capacity [10, 11]. Owing to the excellent properties of AC, including large specific surface area, simple synthesis as well as excellent conductivity, it is the most important and widely used material in the negative

electrode material [12, 13]. Recently, many positive electrode materials, such as transition metal oxides/hydroxides metal sulfides and conducting polymer materials, have been intensively studied for supercapacitors [14, 15]. Among the significant conducting polymers, polypyrrole (PPy) has aroused widespread concern considering its easy synthesis, remarkable storage performance, low price and stability in air [16, 17]. However, the phenomenon of expansion and contraction has limited its further applications to a great degree, always leading to the poor stability and the large internal resistance during the charge and discharge processes. To better solve the issues, many efforts have been concentrated on improving the conductivity and stability of PPy, especially depositing PPy on a carbon-based material with the good conductivity [18, 19].

Reduced graphene oxide (rGO), the distribution of carbon atoms at a 2D monolayer like honeycomb, can be prepared in large quantity through chemical reduction of graphene oxide. Those have attracted great attentions because of the high conductivity, good electrochemical stability, large surface area and remarkable mechanical natures [20, 21]. It is seen that the conductivity of PPy is relatively improved as the formation of PPy/rGO sheets; meanwhile, rGO sheets have provided the nucleation sites for PPy as well as an excellent pathway for electrolyte ion or electron transfer, resulting in good capacitive performance [22]. Therefore, the capacitive property of rGO/PPy compound is evaluated as positive electrode for high-energy device.

In this paper, rGO/PPy compounds are fabricated by one-step oxidation polymerization process in the presence of rGO and pyrrole (Py) with various mass ratios. PPy nanoparticles could directly uniformly coat on the surfaces of rGO sheets. The asymmetric supercapacitors made of rGO/PPy compound and AC can achieve a high energy density of 19.7 Wh kg^{-1} at 478.1 W kg^{-1} with a superior cycling retention rate of 90.9% after 7000 cycles.

2 Experimental procedure

2.1 Materials

Pyrrole, expanded graphite, absolute ethanol, ethylene glycol (EG), activated carbon (AC), polytetrafluoroethylene (PTFE) aqueous solution (60 wt%), acetylene black, hydrochloric acid (HCl), sulfuric acid (H_2SO_4), phosphoric acid (H_3PO_4), potassium permanganate ($KMnO_4$), and sodium sulfate (Na_2SO_4) were purchased from Sinopharm Chemical Reagent Co., Ltd. Sodium p-toluenesulfonate (NaPTSA), ammonium persulfate (APS), and hydrogen peroxide (H_2O_2, 30 wt%) were purchased from Shanghai Aladdin Reagent. Ni foam was from Changsha Liyuan New Material Co., Ltd. All chemicals were employed without further purification.

## 2.2 Preparation of reduced graphene oxide and rGO/PPy compound

Graphene oxide was achieved from graphite according to the improved Hummers' method [23–25]. Ethylene glycol (EG)-reduced rGO was prepared by the Ref. [26]. The detailed steps of prepared rGO are as follows: 100 mg rGO was dispersed into 200 ml of EG and ultrasonically formed a suspension solution for 1 h; Then, the suspension was refluxed overnight at 90 °C; The product was repeatedly washed three times with deionized water and three times with absolute ethanol; Finally, the obtained product was dried in a vacuum oven overnight at 60 °C.

The rGO/PPy compound was prepared with a simple one-pot method combining oxidation with polymerization reaction, as illustrated in Scheme 1. The detailed synthesis process is shown as follows: firstly, the desired rGO and 0.97 g NaPTSA were ultrasonically dispersed in DI water to form a homogeneous solution. Secondly, 1.0-mL Py was added to the above-mentioned solution and stirred vigorously for about 20 min. Finally, the polymerization reaction happened using 0.5 M of APS in an ice bath and the mixture was kept stirring for 1 day. The product was filtered and then washed thoroughly using absolute ethanol and distilled water. After drying overnight, the final rGO/PPy compounds were achieved. For convenience, the achieved products are named as PPy, rGO$_5$/PPy, rGO$_{10}$/PPy, rGO$_{15}$/PPy and rGO$_{20}$/PPy, respectively, on the basis of the various mass ratios of rGO to Py ($r_{GO/Py}$) (0:100, 5:100, 10:100, 15:100 and 20:100).

2.3 Assemble about supercapacitor

Active material, conductive agent and adhesive were mixed with the mass ratio of 17:2:1. Firstly, some alcohol was added to the mixture under strongly stirring to form uniform slurry at 25 °C. Then, press it to form a thin film. Subsequently, the film was cut into a fixed area of the sheet and pressed onto a nickel net. The required working electrode was obtained by drying in vacuum.

The symmetric and asymmetric devices were assembled through using our previous method [27]. A symmetric supercapacitor was fabricated by two as-prepared equal active material electrodes. Before assembling the supercapacitor configuration, activated material electrodes and separator were immersed in 1-M Na_2SO_4 aqueous electrolyte solution for 8 h to make electrolyte homogeneously diffuse into the interior of activated material electrodes. For the asymmetric supercapacitor, the active materials of positive and negative electrodes were rGO$_{10}$/PPy composite and AC, respectively. Based on the CV curves (Fig.

Scheme 1 Illustration of the synthesis process of rGO/PPy
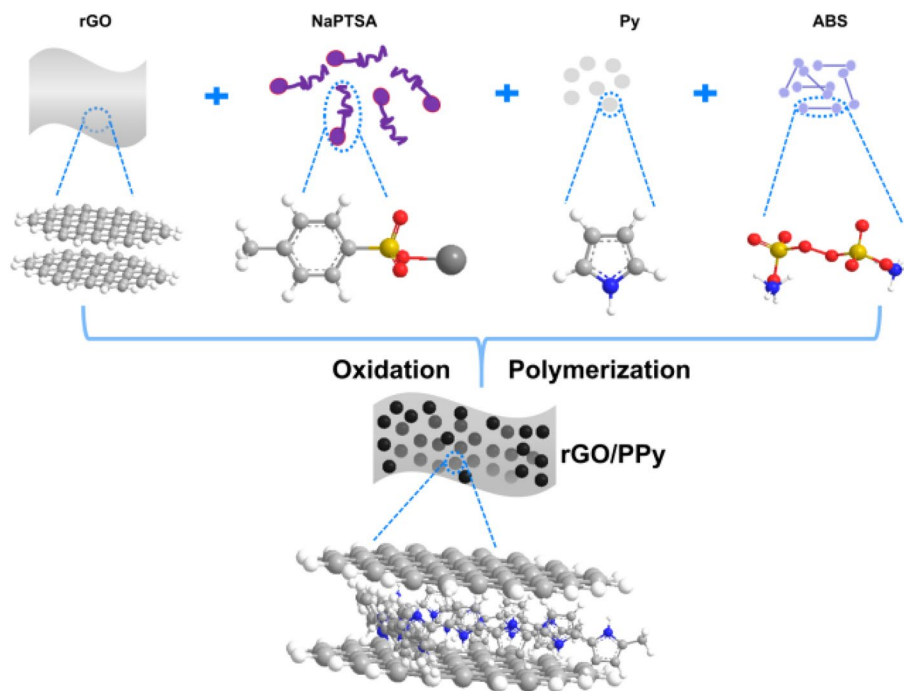
S1), the specific capacitance of the rGO_{10}/PPy composite is 383 F g^{-1}, and the specific capacitance of the AC is 175 F g^{-1}. According to the positive and negative charge balance, the calculated optimal mass ratio of rGO_{10}/PPy composite and AC should be 0.46, which the loading mass of the prepared rGO_{10}/PPy composite and AC is 2.0 and 4.3 mg, respectively. And the electrolyte was also 1-M Na_2SO_4 aqueous solution.

2.4 Characterization

Fourier transformed infrared spectra (FTIR) were tested by a spectrophotometer (8400S, Shimadzu, Japan) pressing into a sheet using KBr particles. X-ray diffraction (XRD) analyses of the obtained materials were measured on an X-ray diffractometer (D8-advance, Bruker, Germany) using a Cu Kα source. The Brunauer–Emmett–Teller (BET) surface area analysis could get data of pore size as well as specific surface area, which used ASAP 2020 Surface Area and Porosity Analyzer (Micromeritics, Norcross, GA, USA). Morphologies and sizes of performed samples can be observed using transmission electron microscopy (TEM, HITACHI H-7650, Japan) and field emission scanning electron microscopy (FESEM, S-4800, Japan) can be observed.

The electrochemical characteristics of assembled supercapacitors were assessed in a two-electrode cell using galvanostatic charge–discharge (GCD), cyclic voltammetry (CV), as well as electrochemical impedance spectroscopy (EIS) tests. The electrochemical workstation (CHI660C, Shanghai ChenHua Co., Ltd, China) is used to determine the electrochemical measurements at 25 °C. The CV data of devices were recorded during 5–100 mV s^{-1} between 0 and 0.8 V and at a voltage ranging from 0.8 to 1.8 V, respectively. Moreover, the GCD curves were collected at 1.0–6.0 A g^{-1}. The EIS tests of devices were performed in 0.01–100,000 Hz.

3 Results and discussion

3.1 Characterization of materials

Figure 1a presents the XRD patterns of rGO, rGO_{10}/PPy compound and PPy. It can be found that the XRD pattern of rGO reveals double sharp diffraction peaks at $2\theta = 25°$ and 43°, which suggests that most hydroxyl and carboxyl groups bonded to graphene nanosheets have been disappeared [28, 29]. The peak of the pure PPy locates at $2\theta = 20–25°$ in accordance with the reported literatures [18, 19]. Furthermore, the XRD pattern of rGO_{10}/PPy compound is almost identical to that of pure PPy. In addition, the peaks from rGO_{10}/PPy compound can be observed the characteristic peaks of rGO and PPy, indicating that rGO and PPy are successfully combined, which is further demonstrated in Fig. 2e, f.

Figure 1b exhibits the FTIR spectra of rGO, rGO_{10}/PPy compound and PPy. It is observed that the peaks at 1240, 1621 and 1725 cm^{-1} are coming from the stretching vibrations of C–O, C=C and C=O of the pure rGO, respectively [19]. The shoulders appear at 1466 and 1547 cm^{-1},
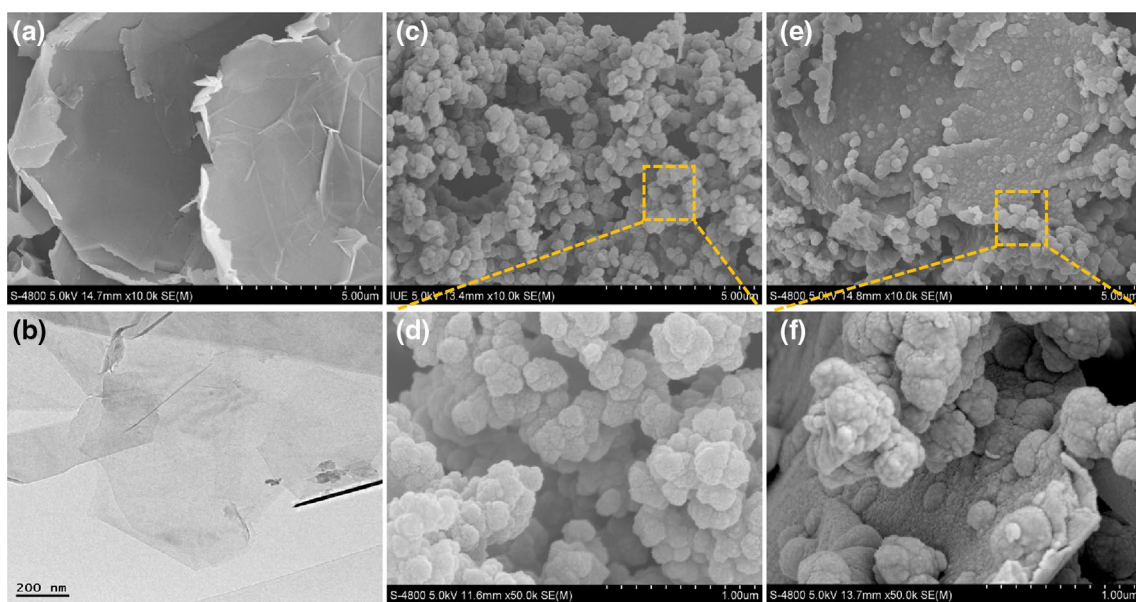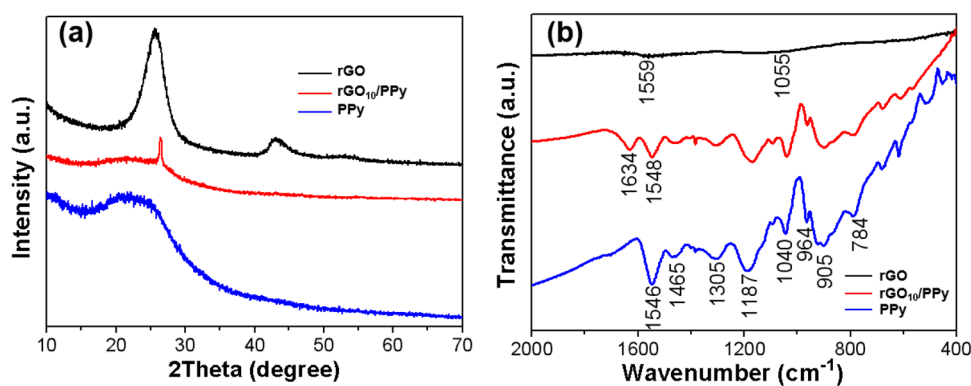
Fig. 2 SEM image (**a**) and TEM image (**b**) of rGO, and SEM images of (**c**, **d**) PPy and (**e**, **f**) rGO$_{10}$/PPy compound

suggesting antisymmetric and symmetric stretching modes of pyrrole ring in PPy FTIR spectrum. The peaks at 1041 and 1306 cm^{-1} are ascribed to the C–H deformation vibrations and C–N stretching vibrations, respectively. Additionally, polymerized pyrrole has typical peaks located at 784 and 964 cm^{-1} [18, 19]. Meanwhile, the existence of PPy can be identified by the peaks located at 1187 and 905 cm^{-1} [18, 19]. In the case of rGO$_{10}$/PPy compound, the peaks belonging to PPy and rGO can be observed easily. Therefore, it can prove that PPy is directly grown on the rGO sheets. From the SEM image of rGO, it exhibits a paper-like structure (Fig. 2a). Figure 2b clearly shows a typical individual rGO sheet which has a lateral dimension of a few micrometers. From the SEM images (Fig. 2c, d), the size of pure PPy particles is approximately 300 nm with some aggregation. The TEM images of rGO$_{10}$/PPy compound (Fig. 2e, f) reveal that the surfaces of rGO sheets are covered with many PPy nanoparticles; besides, little agglomerate of PPy is observed,

which further demonstrates that PPy is indeed grown on the surface of rGO nanosheets via the π–π stacking interactions and van der Waals force.

Figure 3a shows the N$_2$ adsorption–desorption isotherms of as-prepared materials. Hysteresis loops standing for the typical IUPAC type IV sorption feature can be found in all curves, which further suggest the existence of mesoporous structure [30, 31]. The pore size distribution curves (the inset in the Fig. 3a) also prove the above results. Further, it is calculated that the specific surface area increases to 74.0 m^2 g^{-1} with the increasing $r_{rGO/Py}$ from 0:100 to 10:100, as shown in Fig. 3b. The improvement of the specific surface area is caused by the introduction of rGO, which can prevent PPy from aggregating and support for deposition of PPy nanoparticles. This point is favorable for increasing the contact between the electrode and the electrolyte, which may be beneficial to the improvement of the electrochemical performances. Whereas, the specific surface area is reduced

Fig. 3 **a** N_2 adsorption–desorption isotherms, and the inset is pore size distributions of PPy and different rGO/PPy compounds. **b** Influence of $r_{rGO/Py}$ on the specific surface area of material
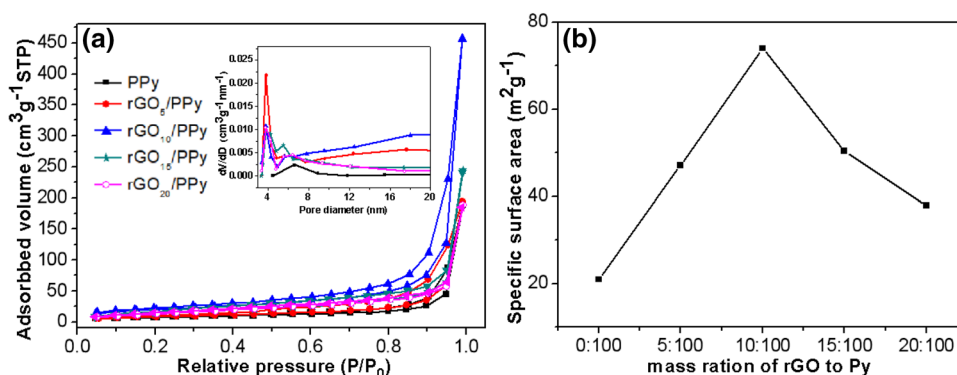
under the further increasing $r_{GO/Py}$, owing to the rGO aggregation. The pore size and specific surface area of AC have been reported in the previous literature [31].

3.2 Electrochemical measurements

To check the effect of rGO and obtain the optimum rGO/PPy composite, the electrochemical performances of rGO, PPy and their composites were investigated in three-electrode system. The CV curves of rGO, PPy and different rGO/PPy composites at a scan rate of 20 mV s^{-1} in 1-M Na_2SO_4 is shown in Fig. 4a. Obviously, the rGO$_{10}$/PPy composite has the largest rectangular area, indicating the highest C_s compared to GO, PPy and their composites. In addition, the GCD test also demonstrates this point, as displayed in Fig. 4b. The rGO$_{10}$/PPy composite has the longest discharging time, which is proportional to C_s. Based on the GCD curves, the rGO$_{10}$/PPy composite obtains the highest C_s of 389.3 F g^{-1} compared to others, as shown in Fig. 4c. To study the practicality of the obtained materials, the measurements such as GCD, CV and EIS are conducted in a two-electrode system. The relationship between $r_{rGO/Py}$ and the electrochemical characteristics of compounds has been studied. Figure 5a shows CV curves of symmetric devices in the voltage range between 0 and 0.8 V at 20 mV s^{-1} based on rGO, PPy and various rGO/PPy compounds. Meanwhile, the CV curves for all samples are similar with rectangular

shape, demonstrating a satisfied capacitive behavior [6]. It is obviously observed that the rGO$_{10}$/PPy compound obtains the largest enclosed area, which suggests the best specific capacitance under the same condition compared with rGO, PPy and other rGO/PPy compounds. Figure 5b displays the GCD curves of different as-prepared materials at 0.25 A g^{-1}. All curves retain almost the same symmetric shape at 0–0.8 V, implying an ideal capacitive character in accordance with the CV curves. The values of iR_{drop} can be calculated according to their GCD curves as shown in Fig. 5c [32, 33]. The ESRs of rGO and PPy are higher than those of compound-based supercapacitors. The reason is the lack of the π–π interaction in PPy and rGO samples. This interaction between rGO nanosheets and the PPy nanoparticles is conducive to extend the conjugation length of the rGO/PPy compound resulting in the improved conductivity, matching with the previous literature [34].The value of ESR is the lowest, when the $r_{rGO/Py}$ is 10:100. Further, the rGO aggregation leads to the enhanced ESR with the increasing $r_{rGO/Py}$. And from their GCD curves, the C_s of rGO, PPy and different rGO/PPy compounds can be evaluated based on the following equations [9, 27]: $C_T = I \times \Delta t/(\Delta V \times m_{ac})$, $C_s = 4 \times C_T$, where C_T (F g^{-1}) refers to specific capacitance of supercapacitor, C_s (F g^{-1}) refers to the single electrode specific capacitance, Δt (s) refers to the discharge time, I (A) refers to the charge/discharge current, ΔV(V) refers to the actual discharging voltage excluding iR_{drop} (V) and m_{ac}
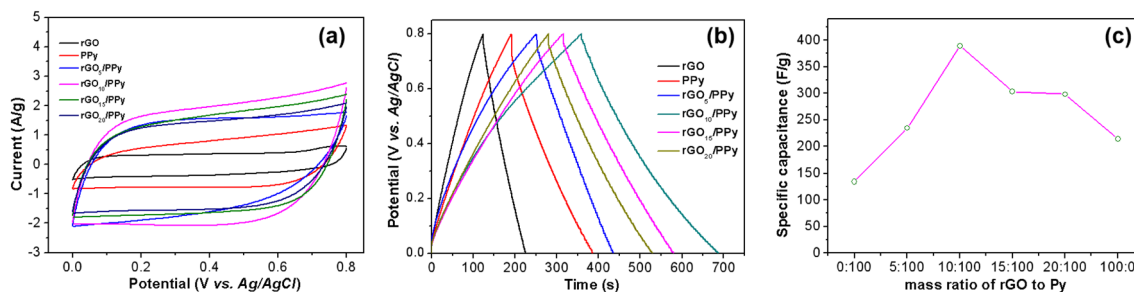

Fig. 4 **a** CV curves of rGO, PPy and their compounds at a scan rate of 20 mV s^{-1} in three-electrode system. **b** GCD curves ofrGO, PPy and their compounds at a constant current density of 1.0 A g^{-1}. **c** C_s based on GCD curves
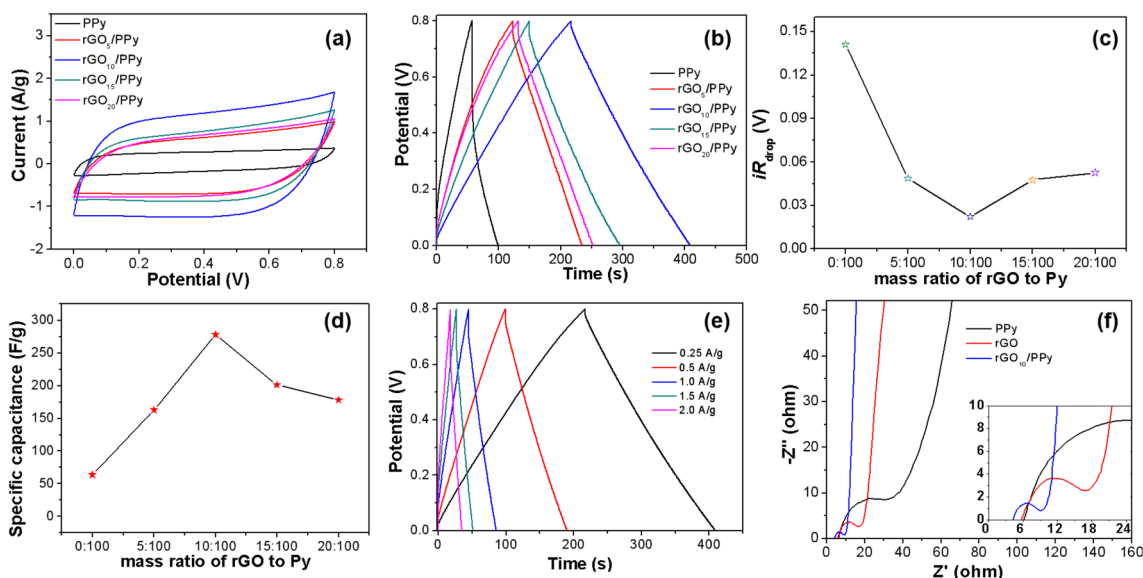
Fig. 5 a CV curves of supercapacitors based on rGO, PPy and different rGO/PPy compounds at a scan rate of 20 mV s^{-1}. **b** GCD curves of supercapacitors based on rGO, PPy and different rGO/PPy compounds at a constant current density of 0.25 A g^{-1}. **c** iR_{drop} and **d** C_s based on GCD curves. **e** GCD curves of supercapacitor based on rGO$_{10}$/PPy compound at different current densities. **f** Nyquist plots of supercapacitors based on rGO, PPy and rGO$_{10}$/PPy compound

(g) represents the total mass. As clearly displayed in Fig. 5d, the C_s values increase sharply with the growth of $r_{rGO/Py}$ and the maximum C_s value is 266.8 F g^{-1} when the $r_{rGO/Py}$ is 10:100. Then, the value of C_s reduces with the further addition of the $r_{rGO/Py}$. Hence, rGO$_{10}$/PPy compound reveals the highest C_s compared to rGO, PPy and other rGO/PPy compounds, due to the three main aspects as follows: (1) the rGO and PPy prevent each other from the agglomeration to obtain higher electrolyte-accessible specific surface area; (2) the right amount of rGO could form the effective conductive network between PPy and rGO promoting the rapid ion transport during the charging/discharging process; and (3) the rGO$_{10}$/PPy electrode displays lower resistance, facilitating the faster electron transfer and ion diffusion.

Figure 5e illustrates the GCD curves of rGO$_{10}$/PPy compound tested between 0 and 0.8 V at different current densities from 0.25 to 2.0 A g^{-1}. The shape of charging curves with straight line is symmetric corresponding to that of the discharging part, implying its remarkable electrochemical reversibility as well as charge/discharge performance during the charge/discharge process. Moreover, the C_s counted from their GCD curves is 266.8 (0.25 A g^{-1}), 260.5 (0.5 A g^{-1}), 249.0 (1.0 A g^{-1}), 240.9 (1.5 A g^{-1}) and 232.1 F g^{-1} (2.0 A g^{-1}), respectively. And it shows that the value of C_s calculated at 2.0 A g^{-1} keeps 87.0% of that calculated at 0.25 A g^{-1}, which testifies that the rGO$_{10}$/PPy compound electrode obtains the high rate capability. The result is attributed to the shortened diffusion/transfer path of ions/electronic, large electrolyte-accessible specific surface area, in favor of improving the conductivity as well as the

close connection between PPy and rGO through π–π stacking interaction and van der Waals force.

The test results of the electrochemical impedance can assess the transfer/diffusion of electronic/ion in the electrode/electrolyte interface, as displayed in Fig. 5f. It is found that all curves appear ideal electrochemical capacitance feature. There is a small depressed semicircle corresponding to the imaginary part at the high-frequency region, as well as the real part at low-frequency region. The rGO$_{10}$/PPy compound presents the best electrochemical impedance performances, which has the lowest internal resistance (R_s, 4.27 Ω) based on the semicircle intersection of the curve on the x axis [9, 27, 35], and owns the smallest charge transfer resistance (R_{ct}, 4.89 Ω), according to the diameter of the obtained semi-circle along the x axis from high- to low-frequency part [35]. Furthermore, the rGO$_{10}$/PPy compound electrode illustrates a line closer to the y axis than the others (rGO and PPy) at the low-frequency part, exhibiting excellent capacitive feature. These results prove the advantageous synergistic effect between the both (rGO and PPy) including (1) alleviating two-component (rGO and PPy) agglomeration; (2) reducing particle size; and (3) enhancing electronic conductivity, which plays a vital part in increasing the electrochemical characteristic of the compounds.

3.3 The performance of asymmetric supercapacitor

Based on the abovementioned results, rGO$_{10}$/PPy compound was selected to construct an asymmetric device to further evaluate its potential application value. Figure 6a displays
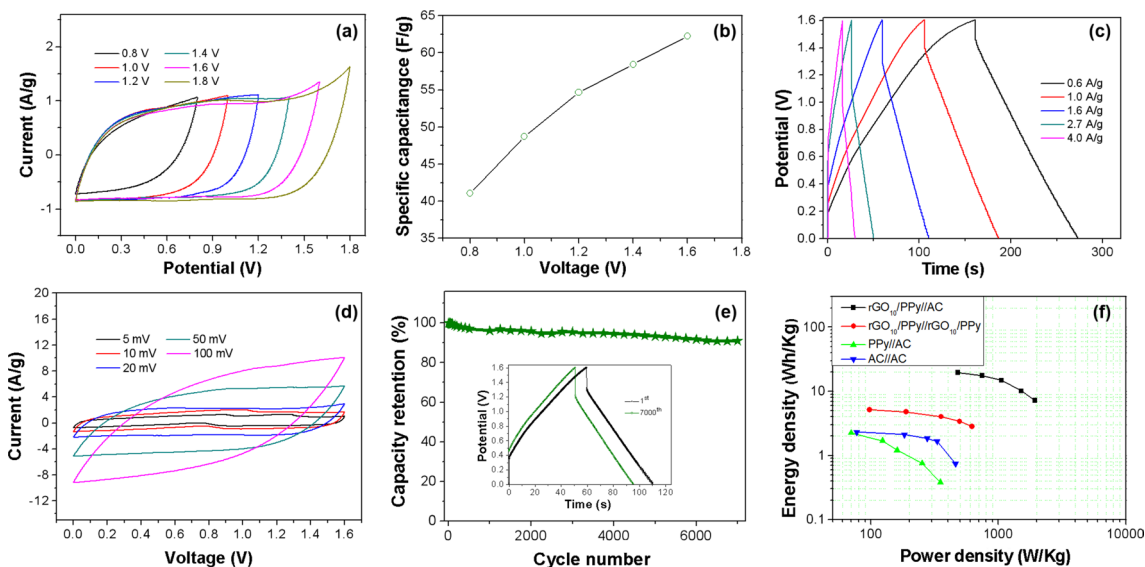
Fig. 6 **a** CV curves of rGO$_{10}$/PPy//AC asymmetric supercapacitor measured at different potential windows in 1-M Na$_2$SO$_4$ aqueous solution at a scan rate of 20 mV s^{-1}. **b** C_T of the asymmetric supercapacitor as a function of potential window. **c** GCD curves and **d** C_T of rGO$_{10}$/PPy//AC asymmetric supercapacitor at different current densi-

ties. **e** Cyclic performances of rGO$_{10}$/PPy//AC asymmetric supercapacitor at current density of 1.6 A g^{-1}, the inset is the GCD curves of the device at 1st, and 7000th cycles. **f** Ragone plots of symmetric and asymmetric supercapacitors based on AC, PPy and rGO$_{10}$/PPy//AC

the typical CV curves of the constructed rGO$_{10}$/PPy//AC asymmetric supercapacitor under various voltage window from 0.8 to 1.8 V at 20 mV s^{-1}. It is well shown that the device possesses quasi-rectangular CV curves with an ideal capacitive characteristic at the voltage window less than or equal to 1.6 V. However, as the voltage range is beyond 1.8 V, it turns out an obvious polarization connected with H$_2$ evolution [36, 37]. Figure 6b illustrates the C_T as a function of voltage range for the device. It can be seen that the C_T is improved remarkably from 41.1 to 62.3 F g^{-1} at 0.8–1.6 V, which implies the advanced stored energy density (*E*) beyond 606% based on the following formula: $E = 1/2CV^2$. The result indicates that the overall property of the device is increased significantly.

The GCD measurements at 0.6–4.0 A g^{-1} are elucidated as shown in Fig. 6c. The charging/discharging curves present symmetric triangular shape and very tiny voltage drops, demonstrating the superior electrochemical reversibility as well as capacitive characteristics. The C_T counted from their GCD curves is 65.9 (0.6 A g^{-1}), 63.0 (1.0 A g^{-1}), 61.3 (1.6 A g^{-1}), 57.7 (2.7 A g^{-1}) and 55.7 F g^{-1} (4.0 A g^{-1}), respectively. It is found that the C_T at 4.0 A g^{-1} has been about 15.5% decay compared with that at 0.6 A g^{-1}, exhibiting the high rate capability of the device belonging to the rGO/PPy compound and AC with high rate performance. In addition, Fig. 6d shows that the value of C_T decreases as the current density increases.

As an important requirement to meet practical applications for the energy storage property, the satisfied long

lift-time is measured and displayed in Fig. 6e. The capacitance of the device can still retain about 90.9% of the initial value after 7000 cycles, demonstrating superior cycling life. This mainly results from the good cyclic stability of the AC. On the other hand, rGO sheets can support PPy nanoparticles and stabilize the structure of PPy, when PPy is severely swelling and shrinking during continuous repeated charging/discharging process.

Both energy density (*E*, Wh kg^{-1}) and power density (*P*, W kg^{-1}) are significant evaluation parameters of device. *E* and *P* of the device can be counted according to the next formulas [9, 27]: $E = 0.5 \times C_T \times (\Delta V)^2/3.6$, $P = E \times 3600/(\Delta t)$. The Ragone plots of rGO$_{10}$/PPy//AC, rGO$_{10}$/PPy//rGO$_{10}$/PPy, AC//AC and PPy//AC devices based on GCD curves are illustrated in Fig. 6f. Obviously, the device can possess a maximum of 19.7 Wh kg^{-1} at 478.1 W kg^{-1}. These results are obviously larger than those supercapacitors, including rGO$_{10}$/PPy//rGO$_{10}$/PPy, AC//AC and PPy//AC. The synergistic effect between two electrodes is beneficial to enhancing *E* and *P* of the device, which is conducive to the formation of the high CT and wide voltage window.

4 Conclusions

This work has demonstrated that the obtained rGO/PPy compounds with various mass ratios of rGO to Py ($r_{rGO/Py}$) for supercapacitors have been prepared through in situ oxidation polymerization. PPy particles have been well coated onto

the surfaces of rGO nanosheets. When the $r_{rGO/Py}$ is 10:100, the rGO/PPy compound presents remarkable capacitive features, including the highest C_s of 389.3 F g^{-1} at 1.0 A g^{-1} in a three-electrode system and 266.8 F g^{-1} at 0.25 A g^{-1} as well as remarkable rate capability in the symmetric supercapacitor system. The excellent performances are ascribed to the improvement of the electrolyte-accessible specific surface area, the effective conductive network between PPy and rGO, as well as the lower resistance facilitating the faster electron transfer and ion diffusion, which result from the advantageous synergistic effect between rGO and PPy. The device is constructed by the rGO$_{10}$/PPy compound and AC as the positive/negative electrode from 0 to 1.6 V, respectively. In addition, the device provides outstanding rate capability with the C_T retention of 84.5% as the addition of current density from 0.6 to 4.0 A g^{-1}. The maximum E of rGO$_{10}$/PPy//AC device is 19.7 Wh kg^{-1} at 478.1 W kg^{-1}. Furthermore, the rGO$_{10}$/PPy//AC device presents the good cyclic stability as well as retains 90.9% of the initial C_T value after 7000 cycles. In addition, a comparative table on the electrochemical performance on some literature of graphene-based materials and their composites considering capacitance, working voltage window, stability, energy density and power density is displayed in supporting information (Table S1†). These encouraging results indicate that such device is expected to satisfy the needs of wide voltage window and outstanding performance energy storage systems.

References

1. Peng LL, Fang ZW, Zhu Y, Yan CS, Yu GH (2018) Holey 2D nanomaterials for electrochemical energy storage. Adv Energy Mater 8:1702179. https://doi.org/10.1002/aenm.201702179

2. Sharma K, Arora A, Tripathi SK (2019) Review of supercapacitors: materials and devices. J Energy Storage 21:801. https://doi.org/10.1016/j.est.2019.01.010

3. Eftekhari A, Li L, Yang Y (2017) Polyaniline supercapacitors. J Power Sources 347:86. https://doi.org/10.1016/j.jpowsour.2017.02.054

4. Meng QF, Cai KF, Chen YX, Chen LD (2017) Research progress on conducting polymer based supercapacitor electrode materials. Nano Energy 36:268. https://doi.org/10.1016/j.nanoen.2017.04.040

5. Fan ZJ, Yan J, Wei T, Zhi LJ, Ning GQ, Li TY, Wei F (2011) Asymmetric supercapacitors based on graphene/MnO$_2$ and activated carbon nanofiber electrodes with high power and energy density. Adv Funct Mater 21:2366–2375. https://doi.org/10.1002/adfm.201100058

6. Dubal DP, Ayyad O, Ruiz V, Gomez-Romero P (2015) Hybrid energy storage: the merging of battery and supercapacitor chemistries. Chem Soc Rev 44:1777. https://doi.org/10.1039/c4cs00266k

7. Jin RC, Meng M, Zhang SH, Yang LX, Li GH (2018) CNTs@C@Cu$_{2-x}$Se hybrid materials: an advanced electrode for high performance lithium batteries and supercapacitors. Energy Technol 6:2179. https://doi.org/10.1002/ente.201800236

8. Zuo WH, Li RZ, Zhou C, Li YY, Xia JL, Liu JP (2017) Battery-supercapacitor hybrid devices: recent progress and future prospects. Adv Sci 4:1600539. https://doi.org/10.1002/advs.201600539

9. Dong J, Jiang YL, Li QD, Wei QL, Yang W, Tan SS, Xu X, An QY, Mai LQ (2017) Pseudocapacitive titanium oxynitride mesoporous nanowires with iso-oriented nanocrystals for ultrahigh-rate sodium ion hybrid capacitors. J Mater Chem A 5:10827. https://doi.org/10.1039/c7ta00463j

10. Ramirez-Castro C, Schütter C, Passerini S, Balducci A (2016) Microporous carbonaceous materials prepared from biowaste for supercapacitor application. Electrochim Acta 206:452. https://doi.org/10.1016/j.electacta.2015.12.126

11. Kandasamy SK, Kandasamy K (2018) Recent advances in electrochemical performances of graphene composite (graphene-polyaniline/polypyrrole/activated carbon/carbon nanotube) electrode materials for supercapacitor: a review. J Inorg Organome P 28:559. https://doi.org/10.1007/s10904-018-0779-x

12. Masikhwa TM, Madito MJ, Bello A, Dangbegnon JK, Manyala N (2017) High performance asymmetric supercapacitor based on molybdenum disulphide/graphene foam and activated carbon from expanded graphite. J Colloid Interf Sci 488:155. https://doi.org/10.1016/j.jcis.2016.10.095

13. Bello A, Barzegar F, Momodu D, Dangbegnon J, Taghizadeh F, Fabiane M, Manyala N (2015) Asymmetric supercapacitor based on nanostructured graphene foam/polyvinyl alcohol/formaldehyde and activated carbon electrodes. J Power Sources 273:305. https://doi.org/10.1016/j.jpowsour.2014.09.094

14. Pazhamalai P, Krishnamoorthy K, Sahoo S, Mariappan VK, Kim S-J (2019) Copper tungsten sulfide anchored on Ni-foam as a high-performance binder free negative electrode for asymmetric supercapacitor. Chem Eng J 359:409. https://doi.org/10.1016/j.cej.2018.11.153

15. Li XQ, Liu YH, Jin ZY, Li PP, Chen XJ, Xiao D (2019) Enhanced electrochemical performance of C-NiO/NiCO$_2$O$_4$//AC asymmetric supercapacitor based on material design and device exploration. Electrochim Acta 296:335. https://doi.org/10.1016/j.electacta.2018.11.011

16. Snook GA, Kao P, Best AS (2011) Conducting-polymer-based supercapacitor devices and electrodes. J Power Sources 196:1. https://doi.org/10.1016/j.jpowsour.2010.06.084

17. Qi K, Hou RZ, Zaman S, Xia BY, Duan HW (2018) A core/shell structured tubular graphene nanoflake-coated polypyrrole hybrid for all-solid-state flexible supercapacitors. J Mater Chem A 6:3913. https://doi.org/10.1039/c7ta11245a

18. Wang JP, Li X, Du XF, Wang J, Ma HR, Jing XL (2017) Polypyrrole composites with carbon materials for supercapacitors. Chem Pap 71:293. https://doi.org/10.1007/s11696-016-0048-9

19. Guo XM, Bai NN, Tian Y, Gai LG (2018) Free-standing reduced graphene oxide/polypyrrole films with enhanced electrochemical performance for flexible supercapacitors. J Power Sources 408:51. https://doi.org/10.1016/j.jpowsour.2018.10.083

20. Kirubasankar B, Murugadoss V, Lin J, Ding T, Dong MY, Liu H, Zhang JX, Li TX, Wang N, Guo ZH, Angaiah S (2018) In situ grown nickel selenide on graphene nanohybrid electrodes for high energy density asymmetric supercapacitors. Nanoscale 10:20414. https://doi.org/10.1039/C8NR06345A

21. Liu CG, Yu ZN, Neff D, Zhamu A, Jang BZ (2010) Graphene-based supercapacitor with an ultrahigh energy density. Nano Lett 10:4863. https://doi.org/10.1021/nl102661q

22. Feng XM, Yan ZZ, Li RM, Liu XF, Hou WH (2013) The synthesis of shape-controlled polypyrrole/graphene and the study

of its capacitance properties. Poly Bull 70:2291. https://doi.org/10.1007/s00289-013-0952-x

23. Marcano DC, Kosynkin DV, Berlin JM, Sinitskii A, Sun ZZ, Slesarev A, Alemany LB, Lu W, Tour JM (2010) Improved synthesis of graphene oxide. ACS Nano 4:4806. https://doi.org/10.1021/nn1006368

24. Zhang YH, Cho UR (2018) Enhanced thermo-physical properties of nitrile-butadiene rubber nanocomposites filled with simultaneously reduced and functionalized graphene oxide. Polym Compos 39:3227. https://doi.org/10.1002/pc.24335

25. Zhang YH, Park S-J (2018) Influence of the nanoscaled hybrid based on nanodiamond@ graphene oxide architecture on the rheological and thermo-physical performances of carboxylated-polymeric composites. Compos Part A Appl S 112:356. https://doi.org/10.1016/j.compositesa.2018.06.020

26. Liu Y, Zhang Y, Ma GH, Wang Z, Liu KY, Liu HT (2013) Ethylene glycol reduced graphene oxide/polypyrrole composite for supercapacitor. Electrochim Acta 88:519. https://doi.org/10.1016/j.electacta.2012.10.082

27. Liu GJ, Wang B, Liu T, Wang L, Luo H, Gao TT, Wang F, Liu AM, Wang DL (2018) 3D self-supported hierarchical core/shell structured $MnCo_2O_4$@CoS arrays for high-energy supercapacitors. J Mater Chem A 6:1822. https://doi.org/10.1039/c7ta10140f

28. Zhu YW, Murali S, Cai WW, Li XS, Suk JW, Potts JR, Ruoff RS (2010) Graphene and graphene oxide: synthesis, properties, and applications. Adv Mater 22:3906. https://doi.org/10.1002/adma.201001068

29. Zhang YH, Park S-J (2018) In situ shear-induced mercapto group-activated graphite nanoplatelets for fabricating mechanically strong and thermally conductive elastomer composites for thermal management applications. Compos Part A Appl Sci 112:40. https://doi.org/10.1016/j.compositesa.2018.06.004

30. Jin RC, Jiang H, Sun YX, Ma YQ, Li HH, Chen G (2016) Fabrication of $NiFe_2O_4$/C hollow spheres constructed by mesoporous nanospheres for high-performance lithium-ion batteries. Chem Eng J 303:501. https://doi.org/10.1016/j.cej.2016.06.032

31. Fan LQ, Liu GJ, Wu JH, Liu L, Lin JM, Wei YL (2014) Asymmetric supercapacitor based on graphene oxide/polypyrrole composite and activated carbon electrodes. Electrochim Acta 137:26. https://doi.org/10.1016/j.electacta.2014.05.137

32. An KH, Kim WS, Park YS, Choi YC, Lee SM, Chung DC, Bae DJ, Lim SC, Lee YH (2001) Supercapacitors using single-walled carbon nanotube electrodes. Adv Mater 13:497. https://doi.org/10.1002/1521-4095(200104)13:7%3c497:AID-ADMA497%3e3.0.CO;2-H

33. Khosrozadeh A, Xing M, Wang Q (2015) A high-capacitance solid-state supercapacitor based on free-standing film of polyaniline and carbon particles. Appl Energy 153:87. https://doi.org/10.1016/j.apenergy.2014.08.046

34. Mo MM, Chen CC, Gao H, Chen MW, Li DG (2018) Wet-spinning assembly of cellulose nanofibers reinforced graphene/polypyrrole microfibers for high performance fiber-shaped supercapacitors. Electrochim Acta 269:11. https://doi.org/10.1016/j.electacta.2018.02.118

35. Wu JH, Yu HJ, Fan LQ, Luo GG, Lin JM, Huang ML (2012) A simple and high-effective electrolyte mediated with p-phenylenediamine for supercapacitor. J Mater Chem 22:19025. https://doi.org/10.1039/c2jm33856d

36. Ml He, Fic K, Fra E, Novák P, Berg EJ (2016) Ageing phenomena in high-voltage aqueous supercapacitors investigated by in situ gas analysis. Energy Environ Sci 9:623. https://doi.org/10.1039/C5EE02875B

37. Khomenko V, Raymundo-Pinero E, Frackowiak E, Beguin F (2006) High-voltage asymmetric supercapacitors operating in aqueous electrolyte. Appl Phys A 82:567. https://doi.org/10.1007/s00339-005-3397-8